Monthly Notices of the ROYAL ASTRONOMICAL SOCIETY

MNRAS **511,** 4766–4773 (2022) https://doi.org/10.1093/mnras/stac251
Advance Access publication 2022 January 29

Filamentation of fast radio bursts in magnetar winds

Emanuele Sobacchi,[1]★ Yuri Lyubarsky,[2] Andrei M. Beloborodov[3,4] and Lorenzo Sironi[1]

[1]*Department of Astronomy and Columbia Astrophysics Laboratory, Columbia University, 550 West 120th Street, New York, NY 10027, USA*
[2]*Department of Physics, Ben-Gurion University, P.O.B. 653, Beer-Sheva 84105, Israel*
[3]*Department of Physics and Columbia Astrophysics Laboratory, Columbia University, 538 West 120th Street, New York, NY 10027, USA*
[4]*Max Planck Institute for Astrophysics, Karl-Schwarzschild-Street 1, D-85741, Garching, Germany*

Accepted 2022 January 25. Received 2022 January 24; in original form 2021 November 9

ABSTRACT

Magnetars are the most promising progenitors of fast radio bursts (FRBs). Strong radio waves propagating through the magnetar wind are subject to non-linear effects, including modulation/filamentation instabilities. We derive the dispersion relation for modulations of strong waves propagating in magnetically dominated pair plasmas focusing on dimensionless strength parameters $a_0 \lesssim 1$, and discuss implications for FRBs. As an effect of the instability, the FRB-radiation intensity develops sheets perpendicular to the direction of the wind magnetic field. When the FRB front expands outside the radius where the instability ends, the radiation sheets are scattered due to diffraction. The FRB-scattering time-scale depends on the properties of the magnetar wind. In a cold wind, the typical scattering time-scale is $\tau_{\rm sc} \sim$ μs–ms at the frequency $\nu \sim 1\,$GHz. The scattering time-scale increases at low frequencies, with the scaling $\tau_{\rm sc} \propto \nu^{-2}$. The frequency-dependent broadening of the brightest pulse of FRB 181112 is consistent with this scaling. From the scattering time-scale of the pulse, one can estimate that the wind Lorentz factor is larger than a few tens. In a warm wind, the scattering time-scale can approach $\tau_{\rm sc} \sim$ ns. Then scattering produces a frequency modulation of the observed intensity with a large bandwidth, $\Delta\nu \sim 1/\tau_{\rm sc} \gtrsim 100\,$MHz. Broad-band frequency modulations observed in FRBs could be due to scattering in a warm magnetar wind.

Key words: instabilities – plasmas – relativistic processes – radio continuum: transients – fast radio bursts.

1 INTRODUCTION

Fast radio bursts (FRBs) are bright flashes of millisecond duration (e.g. Lorimer et al. 2007; Thornton et al. 2013; Spitler et al. 2014, 2016; Petroff et al. 2016; Shannon et al. 2018; CHIME/FRB Collaboration et al. 2019a, b, c). Magnetars are promising progenitors of FRBs. The FRB–magnetar connection, which was initially proposed on statistical grounds (e.g. Popov & Postnov 2010, 2013), is strongly supported by the discovery of weak FRBs from the Galactic magnetar SGR 1935+2154 (e.g. Bochenek et al. 2020; CHIME/FRB Collaboration et al. 2020).

Due to the huge luminosity of FRBs, the electromagnetic field of the radio wave accelerates the electrons in the magnetar wind up to a significant fraction of the speed of light (e.g. Luan & Goldreich 2014). Strong FRB waves can experience non-linear propagation effects, including modulation/filamentation instabilities (Sobacchi et al. 2021).[1] The instability produces a spatial modulation of the intensity of the FRB wave. As the FRB front expands, the structures generated by the instability are scattered due to diffraction, and may interfere with each other. This process leaves an imprint on the time–frequency structure of FRBs.

In our previous work (Sobacchi et al. 2021), we studied the modulation/filamentation instabilities of FRBs propagating in a weakly magnetized electron-ion plasma. Such environment may be found at large distances from the FRB progenitor. The instability develops at nearly constant electron density since the effect of the ponderomotive force is suppressed due to the large inertia of the ions. Then the dominant non-linear effect is the modification of the plasma frequency due to relativistic corrections to the effective electron mass. In regions of enhanced radiation intensity, the plasma frequency decreases because the electrons oscillate with a larger velocity in the field of the wave, and therefore have a larger effective mass. Modulations of the radiation intensity perpendicular to the direction of propagation of the wave grow because the refractive index of the plasma increases, which creates a converging lens that further enhances the radiation intensity. Modulations along the direction of propagation grow because the group velocity of the wave depends on the local radiation intensity. It turns out that the spatial scale of the modulations is shorter along the direction of propagation than in the perpendicular direction.

In this paper, we study the modulation/filamentation of FRBs propagating in a magnetar wind, which is modelled as a magnetically dominated pair plasma. We find that the instability develops because the ponderomotive force pushes particles out of regions of enhanced radiation intensity. The refractive index of the plasma increases in the regions where the particle number density is smaller, thus creating a

★ E-mail: es3808@columbia.edu

[1]Modulation/filamentation instabilities of strong electromagnetic waves propagating in unmagnetized electron-ion plasmas are extensively studied in the field of laser–plasma interaction (e.g. Kruer 2019). Filamentation has been observed in numerical simulations of relativistic magnetized shocks, in which case a strong electromagnetic precursor is emitted upstream (e.g. Iwamoto et al. 2017, 2022; Babul & Sironi 2020; Sironi et al. 2021).

Table 1. Wavenumber in the transverse direction (k_y) and in the longitudinal direction (k_z), and growth rate (Γ) of the unstable modes (the electromagnetic pump wave is propagating along the z direction). Results are the same for a weakly magnetized wind ($\sigma_w \ll a_0^2$), and for a magnetically dominated wind with the background magnetic field along k_y. The growth rate remains same order of the maximal one for $k_z \ll a_0\omega_P/c$, while there is no instability for $k_z \gg a_0\omega_P/c$. When $a_0 \gg \beta_s^2\omega_0/\omega_P$, the growth rate remains same order of the maximal one for $\sqrt{a_0\omega_0\omega_P}/c \ll k_y \ll a_0\beta_s^{-1}\omega_P/c$. Since $k_y \gg k_z$, the modulations are elongated in the direction of propagation of the electromagnetic pump wave.

Range of a_0	ck_y	ck_z	Γ
$a_0 \gg \beta_s^2\omega_0/\omega_P$	$\sqrt{a_0\omega_0\omega_P} \ll ck_y \ll a_0\beta_s^{-1}\omega_P$	$\ll a_0\omega_P$	$a_0\omega_P/\sqrt{2}$
$a_0 \ll \beta_s^2\omega_0/\omega_P$	$ck_y \simeq a_0\beta_s^{-1}\omega_P/2$	$\ll a_0\omega_P$	$a_0^2\beta_s^{-2}\omega_P^2/8\omega_0$

Table 2. Same as Table 1, but for a magnetically dominated wind with the background magnetic field perpendicular to k_y and k_z. The growth rate remains same order of the maximal one for $k_z \ll \omega_L/c$, while there is no instability for $k_z \gg \omega_L/c$.

ck_y	ck_z	Γ
$a_0\omega_P/2$	$\ll\omega_L$	$a_0^2\omega_P^2/8\omega_0$

converging lens that further enhances the radiation intensity. Since the ponderomotive force preferentially pushes particles along the magnetic field lines, the instability produces sheets of radiation intensity perpendicular to the direction of the wind magnetic field. Consistent with previous studies focusing on unmagnetized plasmas (e.g. Kates & Kaup 1989), we do not find significant modulations of the radiation intensity along the direction of the wave propagation.[2]

As the FRB front expands outside the radius where the instability ends, the radiation sheets are diffracted, effectively scattering the arrival time of the FRB wave. In a cold magnetar wind, we find that the scattering time-scale is $\tau_{sc} \sim$ μs–ms. The scattering time is larger at low frequencies,[3] with the scaling $\tau_{sc} \propto \nu^{-2}$. This scaling is consistent with the frequency-dependent broadening of the brightest pulse from FRB 181112 (Cho et al. 2020).

In a warm magnetar wind, the scattering time-scale is much shorter, $\tau_{sc} \sim$ ns. Then scattering produces frequency modulations with a large bandwidth, $\Delta\nu \sim 1/\tau_{sc} \gtrsim 100$ MHz. Such broad-band frequency modulations are often observed in FRBs (e.g. Shannon et al. 2018; Hessels et al. 2019; Nimmo et al. 2021).

The paper is organized as follows. In Section 2, we briefly review some relevant properties of magnetar winds and FRBs. In Section 3, we study the filamentation instability of FRBs. We refer the reader not interested in the technical details of the calculation to Tables 1 and 2, where we summarize our results. In Section 4, we discuss the scattering of FRBs. In Section 5, we conclude.

2 FRBS IN MAGNETAR WINDS

The magnetar wind forms outside the light cylinder, at radii $R \gtrsim R_{LC} = cP/2\pi$, where P is the magnetar rotational period and c is the speed of light. The magnetic field strength in the wind proper frame is $B_{bg} = \mu/\gamma_w R_{LC}^2 R$, where μ is the magnetar magnetic dipole moment, and γ_w is the wind Lorentz factor. The wind magnetic field is nearly azimuthal.

The ratio of the Larmor frequency, $\omega_L = eB_{bg}/mc$, where e is the electron charge, m is the electron mass, and the angular frequency of the FRB wave in the wind frame, $\omega_0 = \pi\nu/\gamma_w$, where ν is the observed frequency, is

$$\frac{\omega_L}{\omega_0} = 2.5\times10^{-4}\mu_{33}P_0^{-2}\nu_9^{-1}R_{15}^{-1}\,, \quad (1)$$

where, we have defined $\mu_{33} \equiv \mu/10^{33}\,\mathrm{G\,cm^3}$, $P_0 \equiv P/1\,\mathrm{s}$, $\nu_9 \equiv \nu/1\,\mathrm{GHz}$, and $R_{15} \equiv R/10^{15}\,\mathrm{cm}$. At the radii where $\omega_L \ll \omega_0$, the electron motion is weakly affected by B_{bg}. The electrons reach a maximum velocity of a_0c, where $a_0 = eE/\omega_0 mc$. We consider radii where $a_0 \lesssim 1$, so that the electrons are subrelativistic. The peak electric field of the wave in the wind frame, E, can be calculated from the isotropic equivalent of the observed FRB luminosity, $L = 2c\gamma_w^2E^2R^2$. One finds

$$a_0 = 2.3\times10^{-2}\,L_{42}^{1/2}\nu_9^{-1}R_{15}^{-1}\,, \quad (2)$$

where, $L_{42} \equiv L/10^{42}\,\mathrm{erg\,s^{-1}}$. The condition $a_0 \lesssim 1$ is satisfied at radii $R \gtrsim 2.3\times10^{13}L_{42}^{1/2}\nu_9^{-1}$ cm. Since $\omega_L/\omega_0 \ll a_0$, the electric field of the FRB wave is larger than the wind magnetic field.

It is useful to define the wind magnetization, σ_w, as twice the ratio of the magnetic and rest mass energy densities of the plasma. One finds

$$\sigma_w = \frac{\omega_L^2}{\omega_P^2}\,, \quad (3)$$

where, $\omega_P = \sqrt{8\pi N_0e^2/m}$ is the plasma frequency (the particle number density is $2N_0$). We consider a magnetically dominated wind with $\sigma_w \gg 1$.

3 FILAMENTATION INSTABILITY

3.1 Fundamental equations

We consider an electromagnetic wave propagating through a magnetized pair plasma, with mean particle number density $2N_0$, and background magnetic field $\boldsymbol{B}_{bg}$. We study the stability of slow, long-wavelength modulation of the initial wave.

The electromagnetic field of the wave can be expressed using the vector potential $\boldsymbol{A}$. We are interested in the regime where the angular frequency of the wave, ω_0, is much larger than both the Larmor frequency, $\omega_L = eB_{bg}/mc$, and the plasma frequency, $\omega_P = \sqrt{8\pi N_0e^2/m}$. When $\omega_0 \gg \omega_L, \omega_P$, the non-linear wave equation is (e.g. Montgomery & Tidman 1964; Sluijter & Montgomery 1965; Ghosh et al. 2021)

$$\frac{\partial^2\boldsymbol{A}}{\partial t^2} - c^2\nabla^2\boldsymbol{A} + \omega_P^2\frac{\langle N\rangle}{N_0}\left(1 - \frac{1}{2}\frac{e^2\langle A^2\rangle}{m^2c^2}\right)\boldsymbol{A} = 0\,, \quad (4)$$

where, $\langle\ldots\rangle$ denotes the average on the spatial scale of many wavelengths of the initial wave. We have defined $\langle N\rangle$ as half the total particle number density, namely $2\langle N\rangle = \langle N_{e^+}\rangle + \langle N_{e^-}\rangle$ where $\langle N_{e^+}\rangle$ and $\langle N_{e^-}\rangle$ are the positron and electron densities. To avoid a lengthy notation, below we write $N_{e^\pm}$ instead of $\langle N_{e^\pm}\rangle$.

Equation (4) contains two non-linear terms. The term proportional to $\langle A^2\rangle$ originates from the relativistic corrections to the effective electron mass, and from the beating between the density oscillations at the frequency $2\omega_0$ and the velocity oscillations at the frequency ω_0 (for a detailed discussion, see appendix A of Ghosh et al. 2021).

[2]Chian & Kennel (1983) argued that strong electromagnetic waves in pair plasmas are modulated along the direction of propagation. However, these authors neglected the effect of the ponderomotive force, which is not justified in pair plasmas.

[3]FRBs may also be scattered by some turbulent plasma screen along the line of sight. In this case, one finds $\tau_{sc} \propto \nu^{-\alpha}$ with $\alpha \sim$ 4–4.4 (e.g. Luan & Goldreich 2014).

The term $\langle N \rangle$ describes plasma-density modulations produced by the ponderomotive force.

We use the same approach that is customarily adopted to study nonlinear propagation effects in unmagnetized electron-ion plasmas (e.g. Kruer 2019). The plasma is described using a two-fluid model. The evolution of the positron and electron number densities is described by the continuity equation:

$$\frac{\partial N_{e^\pm}}{\partial t} + \nabla \cdot (N_{e^\pm} \boldsymbol{V}_{e^\pm}) = 0 \,, \tag{5}$$

where, $\boldsymbol{V}_{e^+}$ and $\boldsymbol{V}_{e^-}$ are the positron and electron coordinate velocities. The evolution of the velocities is described by the Euler's equation:

$$\frac{\partial \boldsymbol{V}_{e^\pm}}{\partial t} + (\boldsymbol{V}_{e^\pm} \cdot \nabla)\, \boldsymbol{V}_{e^\pm} = -c_{\rm s}^2 \frac{\nabla N_{e^\pm}}{N_{e^\pm}} + \pm \frac{e}{m} \left[\boldsymbol{E} + \frac{\boldsymbol{V}_{e^\pm}}{c} \times \left(\boldsymbol{B} + \boldsymbol{B}_{\rm bg} \right) \right] - \frac{1}{2} \frac{e^2}{m^2} \nabla \langle A^2 \rangle \tag{6}$$

where, $c_{\rm s}$ is the thermal velocity. The last term of equation (6) is the gradient of the ponderomotive potential.

The electric field $\boldsymbol{E}$ and the magnetic field $\boldsymbol{B}$ obey Maxwell's equations:

$$\nabla \cdot \boldsymbol{E} = 4\pi e \left(N_{e^+} - N_{e^-} \right) \tag{7}$$

$$\nabla \cdot \boldsymbol{B} = 0 \tag{8}$$

$$\nabla \times \boldsymbol{E} = -\tfrac{1}{c} \tfrac{\partial \boldsymbol{B}}{\partial t} \tag{9}$$

$$\nabla \times \boldsymbol{B} = \tfrac{4\pi}{c} e \left(N_{e^+} \boldsymbol{V}_{e^+} - N_{e^-} \boldsymbol{V}_{e^-} \right) + \tfrac{1}{c} \tfrac{\partial \boldsymbol{E}}{\partial t} \,. \tag{10}$$

We remark that all the physical quantities in equations (5)–(10) describe oscillations at frequencies much smaller than ω_0.

The remainder of this section is organized as follows. In Section 3.2, we find a solution of equations (4)–(10) that is independent of x and y (such solution is called 'electromagnetic pump wave'). In Sections 3.3 and 3.4, we study the stability of the initial pump wave. We focus on the regime of subrelativistic electron motion, i.e. $a_0 = eA_0/mc \lesssim 1$ and $\beta_{\rm s} = c_{\rm s}/c \ll 1$.

3.2 Electromagnetic pump wave

The electromagnetic pump wave is described by the vector potential:

$$\boldsymbol{A} = \frac{1}{2} \boldsymbol{A}_0 \exp\left({\rm i}\omega_0 t - {\rm i}\boldsymbol{k}_0 \cdot \boldsymbol{x} \right) + {\rm c.c.} \,, \tag{11}$$

where, $\boldsymbol{A}_0$ is real, and c.c. indicates the complex conjugate [then equation (11) gives $\boldsymbol{A} = \boldsymbol{A}_0 \cos\left(\omega_0 t - \boldsymbol{k}_0 \cdot \boldsymbol{x}\right)$]. Since $\langle A^2 \rangle = A_0^2/2$, the gradient of the ponderomotive potential vanishes. Then equations (5)–(10) have the straightforward solution $N_{e^\pm} = N_0$, $\boldsymbol{V}_{e^\pm} = 0$, and $\boldsymbol{E} = \boldsymbol{B} = 0$. Substituting equation (11) into equation (4), one finds the dispersion relation of the pump wave:

$$\omega_0^2 = c^2 k_0^2 + \omega_{\rm P}^2 \left(1 - \frac{1}{4} a_0^2 \right) \,, \tag{12}$$

where,

$$a_0 = \frac{e A_0}{mc} \,. \tag{13}$$

Equation (12) is the classical result of Sluijter & Montgomery (1965).

3.3 Small perturbations

Modulations with frequency ω and wave vector $\boldsymbol{k}$ of intensity of the pump wave are described by two beating wavebands with frequencies $\omega_\pm = \omega \pm \omega_0$ and wave vectors $\boldsymbol{k}_\pm = \boldsymbol{k} \pm \boldsymbol{k}_0$, where $\omega^2 \ll \omega_0^2$ and $k^2 \ll k_0^2$. The perturbed vector potential is

$$\boldsymbol{A} = \frac{1}{2} \boldsymbol{A}_0 \exp\left({\rm i}\omega_0 t - {\rm i}\boldsymbol{k}_0 \cdot \boldsymbol{x} \right) + \delta \boldsymbol{A}_+ \exp\left({\rm i}\omega_+ t - {\rm i}\boldsymbol{k}_+ \cdot \boldsymbol{x} \right) + \delta \boldsymbol{A}_- \exp\left({\rm i}\omega_- t - {\rm i}\boldsymbol{k}_- \cdot \boldsymbol{x} \right) + {\rm c.c.}, \tag{14}$$

where, $\boldsymbol{A}_0$ and $\delta \boldsymbol{A}_\pm$ are nearly aligned. Writing $\boldsymbol{A}_0 = A_0 \boldsymbol{n}$ and $\delta \boldsymbol{A}_\pm = \delta A_\pm \boldsymbol{n}$, where $\boldsymbol{n}$ is a unit vector, from equation (14) one finds

$$\langle A^2 \rangle - \frac{1}{2} A_0^2 = A_0 \left(\delta A_+ + \delta A_- \right) \exp\left({\rm i}\omega t - {\rm i}\boldsymbol{k} \cdot \boldsymbol{x} \right) + {\rm c.c.} \,, \tag{15}$$

where, we have neglected quadratic terms in the perturbed quantities. The average is made on a spatial scale much longer than k_0^{-1}, and much shorter than k^{-1}.

Below we use equations (5)–(10) to calculate the density perturbation $\delta N = \delta N_{e^+} + \delta N_{e^-}$ as a function of δA_+ and δA_-. Then we substitute δN into equation (4) and derive two homogeneous equations for δA_+ and δA_-. The condition that the determinant of the coefficients vanishes gives the dispersion relation.

3.3.1 *Two-fluid equations*

Substituting $N_{e^\pm} = N_0 + \delta N_{e^\pm}$, $\boldsymbol{V}_{e^\pm} = \delta \boldsymbol{V}_{e^\pm}$, into equations (5)–(6), and neglecting quadratic terms in the perturbed quantities, one finds

$$\frac{\partial \delta N_{e^\pm}}{\partial t} + N_0 \nabla \cdot \delta \boldsymbol{V}_{e^\pm} = 0 \tag{16}$$

$$\frac{\partial \delta \boldsymbol{V}_{e^\pm}}{\partial t} = -c_{\rm s}^2 \tfrac{\nabla \delta N_{e^\pm}}{N_0} \pm \tfrac{e}{m} \left[\delta \boldsymbol{E} + \tfrac{\delta \boldsymbol{V}_{e^\pm}}{c} \times \boldsymbol{B}_{\rm bg} \right] - \tfrac{1}{2} \tfrac{e^2}{m^2} \nabla \langle A^2 \rangle \,. \tag{17}$$

It is convenient to introduce new variables defined as $2\delta N = \delta N_{e^+} + \delta N_{e^-}$, $2\delta N_{\rm a} = \delta N_{e^+} - \delta N_{e^-}$, $2\delta \boldsymbol{V} = \delta \boldsymbol{V}_{e^+} + \delta \boldsymbol{V}_{e^-}$, and $2\delta \boldsymbol{V}_{\rm a} = \delta \boldsymbol{V}_{e^+} - \delta \boldsymbol{V}_{e^-}$. From equation (16), one finds

$$\frac{\partial \delta N}{\partial t} + N_0 \nabla \cdot \delta \boldsymbol{V} = 0 \tag{18}$$

$$\frac{\partial \delta N_{\rm a}}{\partial t} + N_0 \nabla \cdot \delta \boldsymbol{V}_{\rm a} = 0 \,. \tag{19}$$

From equation (17), one finds

$$\frac{\partial \delta \boldsymbol{V}}{\partial t} = -c_{\rm s}^2 \tfrac{\nabla \delta N}{N_0} + \tfrac{e}{m} \tfrac{\delta \boldsymbol{V}_{\rm a}}{c} \times \boldsymbol{B}_{\rm bg} - \tfrac{1}{2} \tfrac{e^2}{m^2} \nabla \langle A^2 \rangle \tag{20}$$

$$\frac{\partial \delta \boldsymbol{V}_{\rm a}}{\partial t} = -c_{\rm s}^2 \tfrac{\nabla \delta N_{\rm a}}{N_0} + \tfrac{e}{m} \left[\delta \boldsymbol{E} + \tfrac{\delta \boldsymbol{V}}{c} \times \boldsymbol{B}_{\rm bg} \right] \,. \tag{21}$$

Substituting $\boldsymbol{E} = \delta \boldsymbol{E}$, $\boldsymbol{B} = \delta \boldsymbol{B}$ into equations (7)–(10), one finds

$$\nabla \cdot \delta \boldsymbol{E} = 8\pi e \delta N_{\rm a} \tag{22}$$

$$\nabla \cdot \delta \boldsymbol{B} = 0 \tag{23}$$

$$\nabla \times \delta \boldsymbol{E} = -\tfrac{1}{c} \tfrac{\partial \delta \boldsymbol{B}}{\partial t} \tag{24}$$

$$\nabla \times \delta \boldsymbol{B} = \tfrac{8\pi}{c} e N_0 \delta \boldsymbol{V}_{\rm a} + \tfrac{1}{c} \tfrac{\partial \delta \boldsymbol{E}}{\partial t} \,. \tag{25}$$

It is convenient to introduce a system of coordinates (x', y', and z') so that $\boldsymbol{k} = k \boldsymbol{e}_{z'}$ and $\boldsymbol{B}_{\rm bg} = B_{\rm bg} \sin\theta \boldsymbol{e}_{y'} + B_{\rm bg} \cos\theta \boldsymbol{e}_{z'}$. Since $\nabla \langle A^2 \rangle$ is directed along $\boldsymbol{k}$, the solution has the form $\delta \boldsymbol{V} = \delta V_{y'} \boldsymbol{e}_{y'} + \delta V_{z'} \boldsymbol{e}_{z'} +$ c.c., $\delta \boldsymbol{V}_{\rm a} = \delta V_{{\rm a},x'} \boldsymbol{e}_{x'} +$ c.c., $\delta N_{\rm a} = 0$, $\delta \boldsymbol{E} = \delta E_{x'} \boldsymbol{e}_{x'} +$ c.c., and

$\delta \boldsymbol{B} = \delta B_{y'} \boldsymbol{e}_{y'}$ + c.c. Since $\nabla \langle A^2 \rangle$ is proportional to $\exp(\mathrm{i}\omega t - \mathrm{i}\boldsymbol{k} \cdot \boldsymbol{x})$, all the variables depend on the coordinates as $\exp(\mathrm{i}\omega t - \mathrm{i}\boldsymbol{k} \cdot \boldsymbol{x})$.

Equation (24) gives $\delta B_{y'} = (ck/\omega)\delta E_{x'}$. Substituting $\delta B_{y'} = (ck/\omega)\delta E_{x'}$ into equation (25), one finds

$$\frac{e}{m}\delta E_{x'} = \mathrm{i}\frac{\omega\omega_{\mathrm{P}}^2}{\omega^2 - c^2k^2}\delta V_{\mathrm{a},x'} \,. \tag{26}$$

The y' component of equation (20) gives

$$\delta V_{y'} = \mathrm{i}\frac{\omega_{\mathrm{L}}}{\omega}\cos\theta\delta V_{\mathrm{a},x'} \,. \tag{27}$$

Using equations (26)–(27), from equation (21) one finds

$$\sin\theta\delta V_{z'} + \mathrm{i}\frac{\omega}{\omega_{\mathrm{L}}}\left(1 - \frac{\omega_{\mathrm{P}}^2}{\omega^2 - c^2k^2} - \frac{\omega_{\mathrm{L}}^2}{\omega^2}\cos^2\theta\right)\delta V_{\mathrm{a},x'} = 0 \,. \tag{28}$$

Since $\delta N/N_0 = (k/\omega)\delta V_{z'}$, which follows from equation (18), the z' component of equation (20) gives

$$\mathrm{i}\omega\left(1 - \frac{c_{\mathrm{s}}^2k^2}{\omega^2}\right)\delta V_{z'} - \omega_{\mathrm{L}}\sin\theta\delta V_{\mathrm{a},x'} = \frac{\mathrm{i}}{2}\frac{e^2}{m^2}kA_0(\delta A_+ + \delta A_-)\exp(\mathrm{i}\omega t - \mathrm{i}\boldsymbol{k}\cdot\boldsymbol{x}) \,, \tag{29}$$

where, we have used equation (15) to calculate $\nabla\langle A^2\rangle$. Obtaining $\delta V_{z'}$ from equations (28)–(29), and using the fact that $\langle N\rangle/N_0 - 1 = (k/\omega)\delta V_{z'}$ + c.c., one eventually finds

$$\frac{\langle N\rangle}{N_0} - 1 = \frac{Q}{2}\frac{e^2}{m^2c^2}A_0(\delta A_+ + \delta A_-)\exp(\mathrm{i}\omega t - \mathrm{i}\boldsymbol{k}\cdot\boldsymbol{x}) + \text{c.c.}, \tag{30}$$

where,

$$Q = \frac{\frac{c^2k^2}{\omega^2}\left(1 - \frac{\omega_{\mathrm{P}}^2}{\omega^2 - c^2k^2} - \frac{\omega_{\mathrm{L}}^2}{\omega^2}\cos^2\theta\right)}{\left(1 - \frac{c_{\mathrm{s}}^2k^2}{\omega^2}\right)\left(1 - \frac{\omega_{\mathrm{P}}^2}{\omega^2 - c^2k^2} - \frac{\omega_{\mathrm{L}}^2}{\omega^2}\cos^2\theta\right) - \frac{\omega_{\mathrm{L}}^2}{\omega^2}\sin^2\theta} \,. \tag{31}$$

Note that the density perturbation is independent of ω_{L} when the ponderomotive force is aligned with the magnetic field. Indeed, for $\theta = 0$ one finds $Q = c^2k^2/(\omega^2 - c_{\mathrm{s}}^2k^2)$.

3.3.2 *Dispersion relation*

Substituting equations (14), (15), and (30) into equation (4), and neglecting quadratic terms in the perturbed quantities, one finds

$$S_+\exp(\mathrm{i}\omega_+ t - \mathrm{i}\boldsymbol{k}_+\cdot\boldsymbol{x}) + S_-\exp(\mathrm{i}\omega_- t - \mathrm{i}\boldsymbol{k}_-\cdot\boldsymbol{x}) + \text{c.c.} = 0 \,, \tag{32}$$

where,

$$S_\pm = \left[\omega_\pm^2 - c^2k_\pm^2 - \omega_{\mathrm{P}}^2\left(1 - \frac{1}{4}a_0^2\right)\right]\delta A_\pm + \frac{1}{4}(1-Q)a_0^2\omega_{\mathrm{P}}^2(\delta A_+ + \delta A_-) \,. \tag{33}$$

Equation (32) requires $S_+ = S_- = 0$, which is a homogeneous system of two equations for δA_+ and δA_-. The condition that the determinant of the coefficients vanishes gives the dispersion relation. Since $\omega_\pm^2 - c^2k_\pm^2 - \omega_{\mathrm{P}}^2(1 - a_0^2/4) = (\omega^2 - c^2k^2) \pm 2(\omega_0\omega - c^2\boldsymbol{k}_0\cdot\boldsymbol{k})$, which follows from equation (12), the dispersion relation can be presented as

$$4\left(\omega_0\omega - c^2\boldsymbol{k}_0\cdot\boldsymbol{k}\right)^2 = \left(\omega^2 - c^2k^2\right)^2 + \frac{1}{2}(1-Q)a_0^2\omega_{\mathrm{P}}^2\left(\omega^2 - c^2k^2\right) \,, \tag{34}$$

where, a_0 and Q are given by equations (13) and (31).

3.4 Evolution of the wavebands

Below we solve the dispersion relation, equation (34), and show that the wavebands grow exponentially. We are interested in a magnetically dominated magnetar wind with $\sigma_{\mathrm{w}} = \omega_{\mathrm{L}}^2/\omega_{\mathrm{P}}^2 \gg 1$. We focus on a pump wave that propagates in the direction perpendicular to the background magnetic field, as expected since the wind magnetic field is nearly azimuthal. We introduce a system of coordinates (x, y, and z) so that $\boldsymbol{k}_0 = k_0\boldsymbol{e}_z$, $\boldsymbol{k} = k_y\boldsymbol{e}_y + k_z\boldsymbol{e}_z$, and $\boldsymbol{B}_{\mathrm{bg}} = B_{\mathrm{bg},x}\boldsymbol{e}_x + B_{\mathrm{bg},y}\boldsymbol{e}_y$. The cosine of the angle between the ponderomotive force (which is directed along $\boldsymbol{k}$) and the background magnetic field is $\cos^2\theta = k_y^2B_{\mathrm{bg},y}^2/(k_y^2 + k_z^2)(B_{\mathrm{bg},x}^2 + B_{\mathrm{bg},y}^2)$.

3.4.1 *Case* $\omega^2 \gg \omega_{\mathrm{L}}^2$

It is convenient to start with the case $\omega^2 \gg \omega_{\mathrm{L}}^2$, since the background magnetic field does not affect the development of the instability. Indeed, one can approximate $Q \simeq c^2k^2/(\omega^2 - c_{\mathrm{s}}^2k^2)$, which is independent of ω_{L}.[4] Since the dispersion relation depends only on k_z and k^2, when $\omega^2 \gg \omega_{\mathrm{L}}^2$ there is a rotational symmetry about the direction of propagation of the pump wave.

One can find approximate analytical solutions of equation (34) as follows. Far from the resonances, the right-hand side of equation (34) is small. Then the solution can be presented as $\omega = c^2k_0k_z/\omega_0 + \Delta\omega$, with a small $\Delta\omega$. Substituting $\omega = c^2k_0k_z/\omega_0 + \Delta\omega$, the left-hand side of equation (34) becomes $(\omega_0\omega - c^2k_0k_z)^2 = \omega_0^2(\Delta\omega)^2$.

Now, we discuss the approximation of $\omega^2 - c^2k^2$ on the right-hand side of equation (34). Substituting $\omega = c^2k_0k_z/\omega_0 + \Delta\omega$, one finds $\omega^2 - c^2k^2 \simeq -c^2k_y^2 - c^2k_z^2(1 - c^2k_0^2/\omega_0^2)$. We have neglected the terms $(\Delta\omega)^2$ and $ck_z(\Delta\omega)$, which are much smaller than $c^2k_y^2$ (this can be verified a posteriori from equations (37)–(41)). Since $1 - c^2k_0^2/\omega_0^2 \simeq \omega_{\mathrm{P}}^2/\omega_0^2$, one finds $\omega^2 - c^2k^2 \simeq -c^2k_y^2 - c^2k_z^2\omega_{\mathrm{P}}^2/\omega_0^2$.

Finally, we need to approximate Q. We discuss the two cases $\omega^2 \gg c_{\mathrm{s}}^2k^2$ and $\omega^2 \ll c_{\mathrm{s}}^2k^2$ below.[5] When $\omega^2 \gg c_{\mathrm{s}}^2k^2$, one finds $Q \simeq c^2k^2/\omega^2$. When $c^2k_z^2 \ll (\Delta\omega)^2$, one can approximate $Q \simeq c^2k_y^2/(\Delta\omega)^2$ and $\omega^2 - c^2k^2 \simeq -c^2k_y^2$. Then the dispersion relation can be approximated as

$$4\omega_0^2\left(\frac{\Delta\omega}{ck_y}\right)^4 - c^2k_y^2\left(\frac{\Delta\omega}{ck_y}\right)^2 - \frac{1}{2}a_0^2\omega_{\mathrm{P}}^2 = 0 \,. \tag{35}$$

The wavenumber of the most unstable modes is $ck_y \gg \sqrt{a_0\omega_0\omega_{\mathrm{P}}}$, and the corresponding growth rate is determined by $(\Delta\omega)^2 = -a_0^2\omega_{\mathrm{P}}^2/2$. Since $\Delta\omega$ is purely imaginary, the perturbation moves along z with the group velocity of the pump wave, c^2k_0/ω_0. The conditions $c_{\mathrm{s}}^2k^2 \ll \omega^2$ and $c^2k_z^2 \ll (\Delta\omega)^2$ give $c_{\mathrm{s}}k_y \ll a_0\omega_{\mathrm{P}}$ and $ck_z \ll a_0\omega_{\mathrm{P}}$. Following the procedure that we used to derive equation (35), one sees that the instability does not develop for $c^2k_z^2 \gg (\Delta\omega)^2$, which gives $Q \simeq k^2/k_z^2$.

When $\omega^2 \ll c_{\mathrm{s}}^2k^2$, one finds $Q \simeq -c^2/c_{\mathrm{s}}^2$. Then the dispersion relation can be approximated as

$$4\omega_0^2(\Delta\omega)^2 = c^2k_y^2\left(c^2k_y^2 - \frac{1}{2}a_0^2\frac{c^2}{c_{\mathrm{s}}^2}\omega_{\mathrm{P}}^2\right) \,. \tag{36}$$

[4] Since $Q \gg 1$, in equation (4) one has $\delta\langle N\rangle/N_0 \gg (e^2/m^2c^2)\delta\langle A^2\rangle$. Then the density modulations produced by the ponderomotive force are the dominant non-linear effect leading to the exponential growth of the instability.

[5] As discussed by Ghosh et al. (2021), when $\omega^2 \gg c_{\mathrm{s}}^2k^2$ the ponderomotive force is balanced by the electron inertia. The reason is that one may neglect $c_{\mathrm{s}}^2\nabla\delta N/N_0$ with respect to $\partial\delta\boldsymbol{V}/\partial t$ in equation (20). When $\omega^2 \ll c_{\mathrm{s}}^2k^2$, the thermal pressure and the ponderomotive force balance each other since one may neglect $\partial\delta\boldsymbol{V}/\partial t$ with respect to $c_{\mathrm{s}}^2\nabla\delta N/N_0$ in equation (20).

The maximum growth rate of the instability is found when $c^2k_y^2 = a_0^2c^2\omega_P^2/4c_s^2$, which gives $(\Delta\omega)^2 = -a_0^4c^4\omega_P^4/64\omega_0^2c_s^4$. The condition $\omega^2 \ll c_s^2k^2$ requires $(\Delta\omega)^2 \ll c_s^2k_y^2$ and $c^2k_z^2 \ll c_s^2k_y^2$, which give $a_0 \ll c_s^2\omega_0/\omega_P c^2$ and $ck_z \ll a_0\omega_P$, respectively.

The instability is robust since it can be excited over a broad range of wavenumbers. As we show in Appendix A, the instability develops for all wavenumbers $k_y > 0$ in a cold plasma where the dispersion relation is given by equation (35). The instability develops for $0 < k_y < a_0\omega_P/\sqrt{2}c_s$ in a warm plasma where the dispersion relation is given by equation (36).

We summarize our results in equation (37)–(41) below. The growth rate can be estimated as

$$\Gamma \simeq \tfrac{1}{\sqrt{2}}a_0\omega_P \quad \left(a_0 \gg \beta_s^2\omega_0/\omega_P\right) \tag{37}$$

$$\Gamma \simeq \tfrac{1}{8}a_0^2\beta_s^{-2}\tfrac{\omega_P^2}{\omega_0} \quad \left(a_0 \ll \beta_s^2\omega_0/\omega_P\right) \tag{38}$$

where, $\beta_s = c_s/c$. The most unstable transverse wavenumber can be estimated as

$$\frac{\sqrt{a_0\omega_0\omega_P}}{c} \ll k_y \ll a_0\beta_s^{-1}\tfrac{\omega_P}{c} \quad \left(a_0 \gg \beta_s^2\omega_0/\omega_P\right) \tag{39}$$

$$k_y \simeq \tfrac{1}{2}a_0\beta_s^{-1}\tfrac{\omega_P}{c} \quad \left(a_0 \ll \beta_s^2\omega_0/\omega_P\right). \tag{40}$$

When $a_0 \gg \beta_s^2\omega_0/\omega_P$, the growth rate remains same order of the maximal one for $\sqrt{a_0\omega_0\omega_P} \ll ck_y \ll a_0\beta_s^{-1}\omega_P$. The most unstable longitudinal wavenumber can be estimated as

$$k_z \ll a_0\frac{\omega_P}{c}. \tag{41}$$

The growth rate remains same order of the maximal one for $k_z \ll a_0\omega_P/c$, while there is no instability for $k_z \gg a_0\omega_P/c$. Since $k_y \gg k_z$, the modulations are elongated in the direction of propagation of the electromagnetic pump wave (the instability breaks a wave packet into longitudinal filaments). Since $\omega^2 \sim c^2k_z^2 + \Gamma^2 \sim a_0^2\omega_P^2$, the condition $\omega^2 \gg \omega_L^2$ could be satisfied only for a weak magnetization $\sigma_w \ll a_0^2 \lesssim 1$.

The modes described by equations (37)–(41) also exist in unmagnetized electron-ion plasmas (e.g. Drake et al. 1974; Sobacchi et al. 2021), with the only difference that the ion plasma frequency replaces the electron plasma frequency. Our results are consistent with those of Ghosh et al. (2021), who studied the filamentation of electromagnetic waves in unmagnetized pair plasmas.

3.4.2 *Case $\omega^2 \ll \omega_L^2$, with $B_{bg,x} = 0$*

Since $\omega^2 \gg \omega_L^2$ could be satisfied only for a weak magnetization $\sigma_w \ll a_0^2 \lesssim 1$, one should study the case $\omega^2 \ll \omega_L^2$.

When $B_{bg,x} = 0$, the ponderomotive force is nearly parallel to the background magnetic field. Indeed, one finds $\cos^2\theta = k_y^2/(k_y^2 + k_z^2)$, which gives $\theta \sim 0$ for $k_z \ll k_y$. Then one can approximate $Q \simeq c^2k^2/(\omega^2 - c_s^2k^2)$, which is the same as in the weakly magnetized case discussed in the previous section. The most unstable wavenumber and the growth rate are given by equations (37)–(41). These results are summarized in Table 1. Since $\omega^2 \sim c^2k_z^2 + \Gamma^2 \sim a_0^2\omega_P^2$, the condition $\omega^2 \ll \omega_L^2$ is satisfied in a magnetically dominated plasma.

We remark that the wavenumber and the growth rate of the most unstable modes are the same as in the weakly magnetized case. The reason is that the particles can move freely along the background magnetic field under the effect of the ponderomotive force when $\theta \sim 0$.

3.4.3 *Case $\omega^2 \ll \omega_L^2$, with $B_{bg,y} = 0$*

When $B_{bg,y} = 0$, the ponderomotive force is perpendicular to the background magnetic field. For $\cos\theta = 0$, one finds $Q \ll 1$ because ω_L^2 appears only in the denominator of Q, and ω^2, c^2k^2, and ω_P^2 are much smaller than ω_L^2 in magnetically dominated plasmas. For $Q \ll 1$ the dispersion relation can be approximated as

$$4\omega_0^2(\Delta\omega)^2 = \left(c^2k_y^2 + \frac{\omega_P^2}{\omega_0^2}c^2k_z^2\right)\left(c^2k_y^2 + \frac{\omega_P^2}{\omega_0^2}c^2k_z^2 - \frac{1}{2}a_0^2\omega_P^2\right) \tag{42}$$

The condition $\omega^2 \ll \omega_L^2$ gives $c^2k_z^2 \ll \omega_L^2$. Since $(\omega_P^2/\omega_0^2)c^2k_z^2 \ll \omega_P^2\omega_L^2/\omega_0^2 \ll a_0^2\omega_P^2$, the terms proportional to $c^2k_z^2$ can be neglected in equation (42). The wavenumber of the most unstable modes is $c^2k_y^2 = a_0^2\omega_P^2/4$, and the corresponding growth rate is determined by $(\Delta\omega)^2 = -a_0^4\omega_P^4/64\omega_0^2$. We conclude that the growth rate can be estimated as

$$\Gamma \simeq \frac{1}{8}a_0^2\frac{\omega_P^2}{\omega_0} \tag{43}$$

and the most unstable wavenumber can be estimated as

$$k_y \simeq \tfrac{1}{2}a_0\tfrac{\omega_P}{c} \tag{44}$$

$$k_z \ll \tfrac{\omega_L}{c}. \tag{45}$$

These results are summarized in Table 2. Comparing equations (37)–(38) and (43), one sees that the growth rate is faster when the ponderomotive force is nearly parallel to the direction of the background magnetic field. This may explain the formation of density sheets nearly perpendicular to the pre-shock magnetic field in three-dimensional simulations of the relativistic magnetized shocks (Sironi et al. 2021).

In the modes described by equations (43)–(45), the dominant nonlinear effect is the relativistic correction to the electron motion. The effect of the ponderomotive force is suppressed since the particles cannot move in the direction perpendicular to the magnetic field, and the instability develops at nearly constant electron density. The same modes also exist in unmagnetized electron-ion plasmas (e.g. Max, Arons & Langdon 1974; Sobacchi et al. 2021), where the ponderomotive force can be suppressed due to the inertia of the ions.

In magnetically dominated plasmas the particle distribution could be anisotropic. Then the thermal velocity c_s may be different along the magnetic field lines and in the perpendicular direction. Since the unstable wavenumbers and the growth rate are independent of c_s when the ponderomotive force is perpendicular to the background magnetic field, our results depend only on the value of the thermal velocity along the field lines.

4 SCATTERING OF FRBS

We apply these results to the propagation of a FRB through the magnetically dominated magnetar wind. The observed duration of the FRB is $T \sim 1$ ms. Since the FRB light curve is typically variable, we consider the possibility that the burst is made of pulses with duration $\tau < T$, during which the radiation intensity remains constant. We do not assume any specific emission mechanism.

The wind may be thought of as a sequence of plasma slabs of thickness $\Delta R \sim R$ with a decreasing plasma density $n(R)$. The instability develops when:

(i) The longitudinal wavelength of the unstable modes, $\lambda_z \simeq 2\pi/k_z$, is shorter than the length of the pulse in the wind frame, $\ell \simeq 2\gamma_w c\tau$.

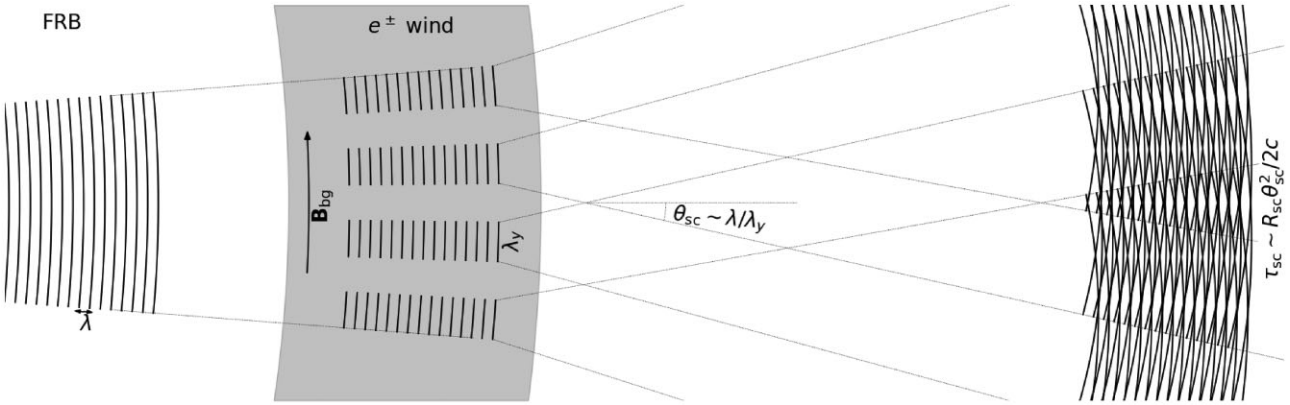

Figure 1. Sketch of the effect of the filamentation instability on the FRB. The magnetar wind (grey region) is pictured as a plasma slab of radius R_{sc} and thickness $\Delta R \sim R_{sc}$ (see equations 46, 48, and 49). The FRB electromagnetic wave (black lines) is broken into sheets of transverse size λ_y, perpendicular to the direction of the wind magnetic field, $\boldsymbol{B}_{bg}$. As the FRB front expands, the radiation sheets are scattered due to diffraction by an angle $\theta_{sc} \sim \lambda/\lambda_y$, where λ is the FRB wavelength in the observer's frame. The corresponding scattering time is $\tau_{sc} \sim R_{sc}\theta_{sc}^2/2c$.

(ii) The time-scale on which the instability grows, $t_{gr} \simeq 10/\Gamma$, is shorter than the expansion time of the wave front in the wind frame, $t_{exp} \simeq R/\gamma_w c$.

The conditions (i) and (ii) are satisfied for $R \lesssim R_1$ and $R \lesssim R_2$, respectively. The values of R_1 and R_2 depend on the thermal velocity, and we calculate them below in the relevant cases.

The instability breaks the wave packet into sheets of radiation perpendicular to the direction of the wind magnetic field. We estimate the transverse size of the radiation sheets as $\lambda_y \simeq 2\pi/k_y$, where $k_y(R)$ is the wavenumber of the most unstable modes.[6] At radii $R \ll \min[R_1, R_2]$, the most unstable transverse wavelength slowly increases with the radius, namely $d\lambda_y/dR \ll \theta_{sc}(R)$, where $\theta_{sc}(R) \sim \lambda/\lambda_y$ is the scattering angle at the radius R (θ_{sc} is measured in the observer's frame), and $\lambda = \pi c/\gamma_w\omega_0$ is the FRB wavelength in the observer's frame.[7] Then the transverse scale of the sheets is gradually adjusted to λ_y. Scattering occurs at a large radius

$$R_{sc} = f \min[R_1, R_2] \ , \tag{46}$$

where, $f \sim 1$ is a numerical factor, since the instability no longer develops for $R \gtrsim R_{sc}$. The corresponding scattering time is $\tau_{sc} \sim R_{sc}\theta_{sc}^2/2c$. The outlined scenario is sketched in Fig. 1.

Different frequency components of the same burst have different scattering times. Since filamentation is a non-linear process, the transverse scale of the sheets, λ_y, depends on the power-weighted frequency of the burst. On the other hand, low-frequency components are more diffracted. The scattering angle is $\theta_{sc} \sim \lambda/\lambda_y \propto \nu^{-1}$, and the corresponding scattering time is $\tau_{sc} \sim R_{sc}\theta_{sc}^2/2c \propto \nu^{-2}$.

We consider the case when the transverse component of the perturbation wave vector is parallel to the wind magnetic field (see Section 3.4.2 and Table 1), which gives the largest growth rate of the instability. First, we discuss the case of a warm plasma, and then the case of a cold plasma.[8]

4.1 Warm magnetar wind

We start considering the case of a warm plasma with $a_0 \ll \beta_s^2\omega_0/\omega_P$, which is satisfied for

$$\begin{aligned}\beta_s &\gg 2\times10^{-3} L_{42}^{1/4}\mu_{33}^{1/2}P_0^{-1}\nu_9^{-1}R_{15}^{-1}\sigma_w^{-1/4} \\ &\sim 8\times10^{-4} L_{42}^{1/4}\dot{N}_{42}^{1/4}\nu_9^{-1}R_{15}^{-1}\gamma_w^{1/4} \ .\end{aligned} \tag{47}$$

We have expressed β_s as a function of the rate of particle outflow in the wind, $\dot{N} \sim L_w/\gamma_w\sigma_w mc^2$, where $L_w \sim \mu^2(2\pi/P)^4/c^3$ is the luminosity of the wind (μ and P are the magnetic dipole moment and the rotational period of the magnetar, γ_w and σ_w are the Lorentz factor and the magnetization of the wind). For our fiducial parameters, we find $\dot{N} \sim 7\times10^{43}\mu_{33}^2P_0^{-4}\gamma_w^{-1}\sigma_w^{-1}\,s^{-1}$. We have defined $\dot{N}_{42} \equiv \dot{N}/10^{42}\,s^{-1}$, which is the appropriate normalization for values of $\gamma_w\sigma_w$ of the order of a few tens, as we find below.

The wavenumbers and the growth rate of the most unstable mode are $ck_y \simeq a_0\beta_s^{-1}\omega_P/2$, $ck_z \lesssim a_0\omega_P$, and $\Gamma \simeq a_0^2\beta_s^{-2}\omega_P^2/8\omega_0$. Then one finds

$$\begin{aligned}R_1 &\sim 2\times10^{15} L_{42}^{1/4}\mu_{33}^{1/2}P_0^{-1}\nu_9^{-1/2}\tau_{-3}^{1/2}\sigma_w^{-1/4}\,cm \\ &\sim 8\times10^{14} L_{42}^{1/4}\dot{N}_{42}^{1/4}\nu_9^{-1/2}\tau_{-3}^{1/2}\gamma_w^{1/4}\,cm\end{aligned} \tag{48}$$

$$\begin{aligned}R_2 &\sim 4\times10^{15} L_{42}^{1/3}\mu_{33}^{2/3}P_0^{-4/3}\nu_9^{-1}\beta_s^{-2/3}\gamma_w^{-2/3}\sigma_w^{-1/3}\,cm \\ &\sim 9\times10^{14} L_{42}^{1/3}\dot{N}_{42}^{1/3}\nu_9^{-1}\beta_s^{-2/3}\gamma_w^{-1/3}\,cm \ ,\end{aligned} \tag{49}$$

where, we have defined $\tau_{-3} \equiv \tau/1$ ms. The conditions $\lambda_z \lesssim \ell$ and $t_{gr} \lesssim t_{exp}$ are satisfied at radii $R \lesssim R_1$ and $R \lesssim R_2$, respectively.

The value of the scattering time depends on the Lorentz factor of the wind. The critical wind Lorentz factor that gives $R_1 = R_2$ is

$$\begin{aligned}\gamma_{cr} &\sim 2\, L_{42}^{1/8}\mu_{33}^{1/4}P_0^{-1/2}\nu_9^{-3/4}\tau_{-3}^{-3/4}\beta_s^{-1}\sigma_w^{-1/8} \\ &\sim L_{42}^{1/7}\dot{N}_{42}^{1/7}\nu_9^{-6/7}\tau_{-3}^{-6/7}\beta_s^{-8/7} \ .\end{aligned} \tag{50}$$

[6]We remark that our estimate relies on an extrapolation of the results of the linear stability analysis, and further investigation is required to understand how the instability saturates.

[7]In a linear wave, transverse modulations of the wave intensity with a scale λ_y result in the deflection of the wave through an angle $\theta_{sc} \sim \lambda/\lambda_y$, which may be thought of as diffraction scattering. Non-linear effects prevent diffraction from occurring at radii $R \ll \max[R_1, R_2]$.

[8]The magnetar wind cools down radiatively and adiabatically. On the other hand, the wind could be heated by magnetic reconnection (e.g. Lyubarsky & Kirk 2001), and by internal shocks (e.g. Beloborodov 2020). We consider the possibility that these processes keep the plasma warm.

Note that $\gamma_{\rm cr} \gg 1$ for $\beta_{\rm s} \ll 1$. When $\gamma_{\rm w} \lesssim \gamma_{\rm cr}$, one finds $R_{\rm sc} = fR_1$, and the scattering time is

$$\tau_{\rm sc} \sim 3\, L_{42}^{1/4} \mu_{33}^{1/2} P_0^{-1} \nu_9^{-5/2} \tau_{-3}^{-3/2} \beta_{\rm s}^{-2} \gamma_{\rm w}^{-2} \sigma_{\rm w}^{-1/4} f^{-3}\ {\rm ns}$$
$$\sim 0.9\, L_{42}^{1/4} \dot{N}_{42}^{1/4} \nu_9^{-5/2} \tau_{-3}^{-3/2} \beta_{\rm s}^{-2} \gamma_{\rm w}^{-7/4} f^{-3}\ {\rm ns}\,. \quad (51)$$

When $\gamma_{\rm w} \gtrsim \gamma_{\rm cr}$, one finds $R_{\rm sc} = fR_2$, and the scattering time is

$$\tau_{\rm sc} \sim 0.8\, \nu_9^{-1} f^{-3}\ {\rm ns}\,. \quad (52)$$

Scattering in a warm wind produces a frequency modulation with a large bandwidth, $\Delta\nu \sim 1/\tau_{\rm sc} \gtrsim 100\,{\rm MHz}$ (see equations 51 and 52). Such broad-band frequency modulations are observed in FRBs (e.g. Shannon et al. 2018; Hessels et al. 2019; Nimmo et al. 2021). The bandwidth increases with the burst frequency (equations 51 and 52 give $\Delta\nu \propto \nu^{\beta}$ with $\beta \sim$ 1–2.5), consistent with observations of FRB 121102 (Hessels et al. 2019).

When the transverse component of the perturbation wave vector is perpendicular to the wind magnetic field (see Section 3.4.3 and Table 2), the unstable modes have $ck_y \simeq a_0\omega_{\rm P}/2$, $ck_z \lesssim \omega_{\rm L}$, and $\Gamma \simeq a_0^2\omega_{\rm P}^2/8\omega_0$. Since the condition $\lambda_z \lesssim \ell$ is easily satisfied, one finds $R_{\rm sc} = fR_2$. The scattering time is the same as in equation (52), regardless of $\beta_{\rm s}$.

4.2 Cold magnetar wind

In a cold plasma with $a_0 \gg \beta_{\rm s}^2\omega_0/\omega_{\rm P}$, we have $ck_z \lesssim a_0\omega_{\rm P}$ and $\Gamma \simeq a_0\omega_{\rm P}/\sqrt{2}$. Since the condition $t_{\rm gr} \lesssim t_{\rm exp}$ is easily satisfied, one finds $R_{\rm sc} = fR_1$. The growth rate remains same order of the maximal one for the transverse wavenumbers $\sqrt{a_0\omega_0\omega_{\rm P}} \lesssim ck_y \lesssim a_0\beta_{\rm s}^{-1}\omega_{\rm P}$. To determine the dominant transverse scale of the radiation sheets, λ_y, one should study how the instability saturates for various wavenumbers, which is out of the scope of the paper. Nevertheless, our results can be used to place a lower limit on the Lorentz factor of the magnetar wind. Since $\lambda_y \lesssim 2\pi c/\sqrt{a_0\omega_0\omega_{\rm P}}$, one finds a lower limit for the scattering time that is independent of $\beta_{\rm s}$,

$$\tau_{\rm sc} \gtrsim 10\, L_{42}^{1/4} \mu_{33}^{1/2} P_0^{-1} \nu_9^{-1/2} \tau_{-3}^{-1/2} \gamma_{\rm w}^{-2} \sigma_{\rm w}^{-1/4} f^{-1}\ {\rm ms}$$
$$\sim 4\, L_{42}^{1/4} \dot{N}_{42}^{1/4} \nu_9^{-1/2} \tau_{-3}^{-1/2} \gamma_{\rm w}^{-7/4} f^{-1}\ {\rm ms}\,. \quad (53)$$

We remark that ν_9 corresponds to the power-weighted frequency of the burst. As discussed above, the frequency components of one burst have different scattering times, with $\tau_{\rm sc} \propto \nu^{-2}$.

Interestingly, the frequency-dependent broadening of the brightest pulse from FRB 181112 is consistent with $\tau_{\rm sc} \propto \nu^{-2}$ (Cho et al. 2020). The rise time of the pulse is $\tau \sim 15$ μs, and the scattering time is $\tau_{\rm sc} \sim 25$ μs. The observed scattering can be an effect of propagation through a cold magnetar wind. Substituting $\tau \sim 15$ μs and $\tau_{\rm sc} \sim 25$ μs into equation (53), one can estimate the wind Lorentz factor,

$$\gamma_{\rm w} \gtrsim 60\, L_{42}^{1/8} \mu_{33}^{1/4} P_0^{-1/2} \nu_9^{-1/4} \sigma_{\rm w}^{-1/8} f^{-1/2}$$
$$\sim 50\, L_{42}^{1/7} \dot{N}_{42}^{1/7} \nu_9^{-2/7} f^{-4/7}\,. \quad (54)$$

This Lorentz factor is not far from $\gamma_{\rm w} \sim$ 10–30 estimated for magnetar winds (Beloborodov 2020).

5 CONCLUSIONS

We have studied the modulation/filamentation instabilities of FRBs propagating in a magnetar wind. We have modelled the wind as a magnetically dominated pair plasma. We have focused on the regime of subrelativistic electron motion, i.e. dimensionless-wave strength parameter $a_0 \lesssim 1$.

The instability modulates the intensity of the radio wave, producing radiation sheets perpendicular to the direction of the wind magnetic field. As the FRB front expands outside the radius where the instability ends, the radiation sheets are diffracted, effectively spreading the arrival time of the FRB wave. The imprint of the scattering on the time–frequency structure of FRBs depends on the properties of the wind.

In a cold wind with $\beta_{\rm s} \ll 10^{-3}$ ($\beta_{\rm s} = c_{\rm s}/c$ is the ratio of the thermal velocity along the magnetic field lines and the speed of light), the typical FRB scattering time is $\tau_{\rm sc} \sim$ μs–ms at the frequency $\nu \sim 1\,{\rm GHz}$. Low frequencies have longer scattering times, with $\tau_{\rm sc} \propto \nu^{-2}$. Such frequency-dependent broadening has been observed in the brightest pulse of FRB 181112 (Cho et al. 2020). From the rise and scattering time-scales of the pulse, we estimate the wind Lorentz factor, $\gamma_{\rm w} \gtrsim 50$. Within the accuracy of this estimate (a factor of a few), $\gamma_{\rm w}$ is consistent with theoretical expectations for magnetar winds (Beloborodov 2020).

In a warm wind with $\beta_{\rm s} \gg 10^{-3}$, the FRB scattering time can approach $\tau_{\rm sc} \sim$ ns. Then scattering produces a frequency modulation of the observed intensity with a large bandwidth, $\Delta\nu \sim 1/\tau_{\rm sc} \gtrsim 100\,{\rm MHz}$. The modulation bandwidth increases with the burst frequency. Broad-band frequency modulations observed in FRBs (e.g. Shannon et al. 2018; Hessels et al. 2019; Nimmo et al. 2021) could be due to scattering in a warm magnetar wind.

ACKNOWLEDGEMENTS

We thank the anonymous referee for constructive comments and suggestions that improved the paper. We acknowledge fruitful discussions with Masanori Iwamoto. YL acknowledges support from the Israel Science Foundation (grant 2067/19). AMB acknowledges support from the Simons Foundation (grant #446228), the Humboldt Foundation, and NSF (AST-2009453). LS acknowledges support from the Sloan Fellowship, the Cottrell Scholars Award, NASA 80NSSC20K1556, NASA 80NSSC18K1104, and NSF AST-1716567.

DATA AVAILABILITY

No new data were generated or analysed in support of this research.

REFERENCES

Babul A.-N., Sironi L., 2020, MNRAS, 499, 2884
Beloborodov A. M., 2020, ApJ, 896, 142
Bochenek C. D., Ravi V., Belov K. V., Hallinan G., Kocz J., Kulkarni S. R., McKenna D. L., 2020, Nature, 587, 59
Chian A. C. L., Kennel C. F., 1983, Ap&SS, 97, 9
CHIME/FRB Collaboration et al., 2019a, Nature, 566, 235
CHIME/FRB Collaboration et al., 2019b, Nature, 566, 230
CHIME/FRB Collaboration et al., 2019c, ApJ, 885, L24
CHIME/FRB Collaboration et al., 2020, Nature, 587, 54
Cho H. et al., 2020, ApJ, 891, L38
Drake J. F., Kaw P. K., Lee Y. C., Schmid G., Liu C. S., Rosenbluth M. N., 1974, Phys. Fluids, 17, 778
Ghosh A., Kagan D., Keshet U., Lyubarsky Y., 2021, preprint (arXiv:2111.00656)
Hessels J. W. T. et al., 2019, ApJ, 876, L23
Iwamoto M., Amano T., Hoshino M., Matsumoto Y., 2017, ApJ, 840, 52
Iwamoto M., Amano T., Matsumoto Y., Matsukiyo S., Hoshino M., 2022, ApJ, 924, 108
Kates R. E., Kaup D. J., 1989, J. Plasma Phys., 42, 507
Kruer W., 2019, The Physics of Laser Plasma Interactions. CRC Press, Boca Raton, Florida
Lorimer D. R., Bailes M., McLaughlin M. A., Narkevic D. J., Crawford F., 2007, Science, 318, 777

Luan J., Goldreich P., 2014, ApJ, 785, L26
Lyubarsky Y., Kirk J. G., 2001, ApJ, 547, 437
Max C. E., Arons J., Langdon A. B., 1974, Phys. Rev. Lett., 33, 209
Montgomery D., Tidman D. A., 1964, Phys. Fluids, 7, 242
Nimmo K. et al., 2021, preprint (arXiv:2105.11446)
Petroff E. et al., 2016, Publ. Astron. Soc. Aust., 33, e045
Popov S. B., Postnov K. A., 2010, in Harutyunian H. A., Mickaelian A. M., Terzian Y., eds, Evolution of Cosmic Objects through their Physical Activity. Gitutyun Publ. House NAS RA, Yerevan, p. 129
Popov S. B., Postnov K. A., 2013, preprint (arXiv:1307.4924)
Shannon R. M. et al., 2018, Nature, 562, 386
Sironi L., Plotnikov I., Nättilä J., Beloborodov A. M., 2021, Phys. Rev. Lett., 127, 035101
Sluijter F. W., Montgomery D., 1965, Phys. Fluids, 8, 551
Sobacchi E., Lyubarsky Y., Beloborodov A. M., Sironi L., 2021, MNRAS, 500, 272
Spitler L. G. et al., 2014, ApJ, 790, 101
Spitler L. G. et al., 2016, Nature, 531, 202
Thornton D. et al., 2013, Science, 341, 53

APPENDIX: SOLUTION OF EQUATIONS (35), (36), AND (42)

We start with the case when the ponderomotive force is nearly parallel to the background magnetic field. In a cold plasma, the dispersion relation is given by equation (35). The growth rate of the exponentially growing solution can be presented as

$$(\Delta\omega)^2 = -\frac{2\Gamma_{\rm cold}^2}{1+\sqrt{1+\frac{k_{\rm cold}^2}{k_y^2}}}\,, \tag{A1}$$

where, $\Gamma_{\rm cold} = a_0\omega_{\rm P}/2$ and $ck_{\rm cold} = \sqrt[4]{8}\sqrt{a_0\omega_0\omega_{\rm P}}$. The maximal growth rate $\Gamma_{\rm cold}$ is achieved for $k_y \gg k_{\rm cold}$. In the top panel of Fig. A1, we plot $\mathrm{Im}(\Delta\omega)/\Gamma_{\rm cold}$ as a function of $k_y/k_{\rm cold}$. The instability develops for all k_y.

In a warm plasma, the dispersion relation is given by equation (36). The solution can be presented as

$$(\Delta\omega)^2 = -\Gamma_{\rm warm}^2\left[1-\left(1-\frac{k_y^2}{k_{\rm warm}^2}\right)^2\right]\,, \tag{A2}$$

where, $\Gamma_{\rm warm} = a_0^2\beta_{\rm s}^{-2}\omega_{\rm P}^2/8\omega_0$ and $ck_{\rm warm} = a_0\beta_{\rm s}^{-1}\omega_{\rm P}/2$. The maximal growth rate $\Gamma_{\rm warm}$ is achieved for $k_y = k_{\rm warm}$. In the bottom panel of Fig. A1, we plot $\mathrm{Im}(\Delta\omega)/\Gamma_{\rm warm}$ as a function of $k_y/k_{\rm warm}$. The instability develops for $k_y < \sqrt{2}k_{\rm warm}$.

When the ponderomotive force is perpendicular to the background magnetic field, the dispersion relation is given by equation (42). The terms proportional to k_z^2 are negligibly small. Then equation (42) is identical to equation (36) after the formal substitution $c_{\rm s} \to c$ in equation (36). The dependence of $\mathrm{Im}(\Delta\omega)$ on k_y is analogous to the bottom panel of Fig. A1.

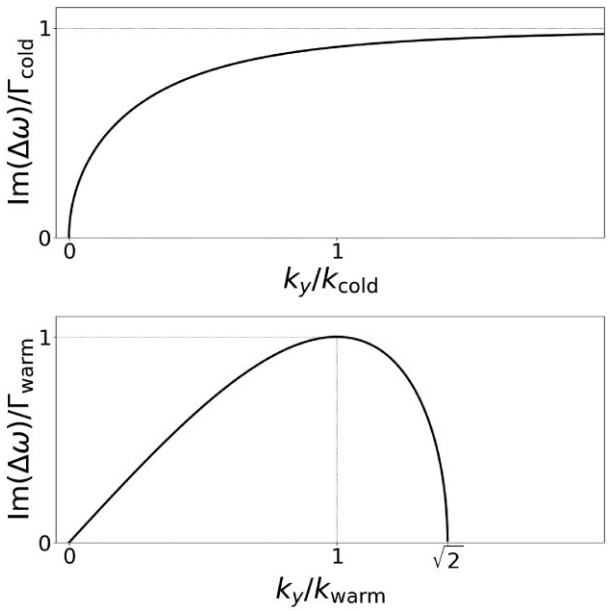

Figure A1. Imaginary part of $\Delta\omega$ as a function of k_y in a cold plasma (top panel) and in a warm plasma (bottom panel). The ponderomotive force is nearly parallel to the background magnetic field.

This paper has been typeset from a TEX/LATEX file prepared by the author.